A simulation strategy for fatigue modeling of delamination in composite structures under multiple loading conditions considering loading history and R-curve effects

Leciñana, I.; Carreras, L.; Renart, J.; Zurbitu, J.; Tijs, B. H.A.H.; Turon, A.

DOI
10.1016/j.compositesa.2024.108402

Publication date
2024

Document Version
Final published version

Published in
Composites Part A: Applied Science and Manufacturing

Citation (APA)
Leciñana, I., Carreras, L., Renart, J., Zurbitu, J., Tijs, B. H. A. H., & Turon, A. (2024). A simulation strategy for fatigue modeling of delamination in composite structures under multiple loading conditions considering loading history and R-curve effects. *Composites Part A: Applied Science and Manufacturing*, *186*, Article 108402. https://doi.org/10.1016/j.compositesa.2024.108402

Composites: Part A 186 (2024) 108402

Contents lists available at ScienceDirect

Composites Part A

journal homepage: www.elsevier.com/locate/compositesa

A simulation strategy for fatigue modeling of delamination in composite structures under multiple loading conditions considering loading history and $\mathcal{R}$-curve effects

I. Leciñana [a,b], L. Carreras [b,*], J. Renart [b], J. Zurbitu [a], B.H.A.H. Tijs [c,d], A. Turon [b]

[a] IKERLAN Technology Research Centre, Basque Research and Technology Alliance (BRTA), Gipuzkoa, Spain
[b] AMADE, Polytechnic School, University of Girona, C/Universitat de Girona 4, 17003 Girona, Spain
[c] GKN Fokker Aerospace, Anthony Fokkerweg 4, 3351 JN Papendrecht, The Netherlands
[d] Faculty of Aerospace Engineering, Delft University of Technology, Kluyverweg 1, 2629 HS Delft, The Netherlands

ARTICLE INFO

Keywords:
Benchmark test
Non-self-similar delamination
Failure mechanism
R-curve effect
Loading history

ABSTRACT

This work evaluates the ability of cohesive zone modeling-based approaches to predict delamination in composite materials that develop large process zones under complex loading conditions. The $\mathcal{R}$-curve effects subjected to static and fatigue loading under multiple loading modes, considering the loading history, are analyzed. To this end, the delamination predictions of a state-of-the-art CZM-based simulation strategy are evaluated by blind simulation of a validation benchmark test. The validation test promotes a non-self-similar delamination scenario, including a process zone that evolves under different loading mode conditions with a non-straight leading delamination front. Good delamination prediction accuracy is achieved. In addition, insights into the relationship between the features of the simulation strategy and the physics of the delamination process are discussed. With regard to the limitations of the simulation strategy, particular attention should be paid to modeling the contribution of an evolving process zone based on the loading mode history.

1. Introduction

The need to be cost-effective and sustainable has become a significant factor in the aeronautical and automotive industries, driving them to focus on creating lighter structures. As a result, there is a growing use of fiber-reinforced polymers (FRP) in these industrial sectors. Among the various resins employed in FRP, the next generation of thermoplastic polymers has the potential to enhance sustainability in the transportation industry when applied with innovative manufacturing methods. In addition, thermoplastic polymers exhibit superior resistance to damage from impacts and enhanced environmental and mechanical resistance compared to thermoset materials [1]. This is attributed to the activation of additional energy-dissipating damage mechanisms apart from brittle fracture. As damage progresses in these materials, large process zones emerge, increasing the fracture toughness as the process zone develops ($\mathcal{R}$-curve) [2].

Apart from the use of new materials, the industry is adopting new approaches to reduce costs, such as high-fidelity modeling-based optimization methodologies and virtual testing [3,4]. To implement these approaches for the new materials with large process zones, the industry must verify that the existing state-of-the-art simulation strategies can accurately model delamination in complex structures under various loading conditions.

The geometry of laminated composite structures, or the location in which the load is applied, may cause the delamination to grow at different rates along the delamination front, forming an arbitrarily shaped delamination front. Moreover, delamination is characterized by a series of microscopic failure events that occur in a region rather than in a localized front, introducing the concept of a non-negligible damage process zone (DPZ). Combining the arbitrarily shaped delamination and the non-negligible damage process zone concepts results in that different material points within the DPZ may have different growing directions [5]. Additionally, the delamination can evolve, driven by both static and/or fatigue loading, under different loading modes. These loading conditions can be combined or applied sequentially during the same delamination process. On a micro-structural scale, damage events progressively occur to resist specific loading conditions. Thus, when the loading conditions that led to the formation of a particular process zone undergo sudden changes, the morphology of the existing DPZ may not be optimal to withstand the altered loading conditions.

* Corresponding author.
E-mail address: laura.carreras@udg.edu (L. Carreras).

https://doi.org/10.1016/j.compositesa.2024.108402
Received 31 January 2024; Received in revised form 23 July 2024; Accepted 5 August 2024
Available online 10 August 2024

All these aspects make the cohesive zone modeling (CZM) [6] an excellent candidate to be used as the core of a simulation tool for delamination prediction at the mesoscale, compared to other widely used methods such as the linear elastic fracture mechanics (LEFM) based virtual crack closure technique (VCCT) [7,8]. CZM shows lower mesh dependency when modeling orthotropic and bi-material interfaces [9], considers the process zone in the wake of the delamination front, and does not require orthogonality of the mesh with the crack geometry.

However, the CZM formulation needs to possess a set of essential capabilities for accurate delamination prediction. These include:(i) the ability to model both static and fatigue delamination under different loading modes; (ii) the capability to capture the onset and the evolution of large damage process zones, including their impact on delamination resistance ($\mathcal{R}$-curve) under static and fatigue loading; and (iii) the ability to take into account the loading history, especially when the mode ratio undergoes changes. These aspects rely on maintaining a consistent formulation and employing suitable and robust approaches to experimentally characterize the cohesive law under various loading modes. Under static loading, a formulation was developed in [10–12], which has been recently extended for its use in the presence of large fracture process zones [13]. From an experimental point of view, there also exist methods to determine the cohesive law, either using the direct method introduced by Sørensen et al. [14,15], or using indirect methods [16–26].

Under fatigue loading, the models available incorporate an evolution of the interface damage with the loading cycles. The first models that appeared [27] did not establish a direct link between this evolution and the experimental evidence, while subsequent formulations already incorporate this evolution either from the crack growth rate, based on a Paris law approach [28–33] or from the S–N curve [34,35]. One of the advantages of the formulation developed in [34,35] is that it is evaluated pointwise, conversely to the formulations that depend on non-local information [32,33]. However, it was found in [35] that a single S–N curve can yield different crack growth rates, so different Paris law coefficients (C), and that the fatigue response is influenced by fatigue parameters and the static cohesive law [36]. This issue was solved in [37], where a robust fatigue parameter determination method was developed to obtain the fatigue inputs for the model from onset and crack growth rate curves and the static cohesive law.

When modeling large process zones, additional energy-dissipating mechanisms besides the typical brittle fracture must be considered. These mechanisms increase the fracture toughness of the interface as the delamination process evolves ($\mathcal{R}$-curve). A more complex shape than the basic bi-linear cohesive law is needed to capture this $\mathcal{R}$-curve. An efficient and simple method to avoid using complex cohesive law shapes [13,21] is to superpose multiple bi-linear cohesive laws to capture the contribution of the different damage mechanisms, as proposed in [38]. The integral of the cohesive law envelope that results from the addition of the multiple superposed cohesive laws correlates with the material's $\mathcal{R}$-curve.

Materials with large process zones develop different energy-diss ipating mechanisms as a function of the applied loading conditions. The physics behind each damage mechanism is defined as a consequence of the fact that the damage gets developed following the path from which the dissipated energy is minimal. For example, bridging fibers under mode I loading requires less energy than fiber breakage. Under shear mode loading, the shear cusp formation maximizes delamination resistance, minimizing the released energy [39]. Under fatigue loading, the activation of additional damage mechanism is also a function of the available energy in the fatigue cycle [40,41]. However, the delamination resistance contribution of an already developed delamination process zone if the loading conditions suddenly change is not well analyzed in the literature. According to the author's best knowledge, there is no CZM formulation that considers the resistance capacity of a developed large process zone as a function of the loading history. In fact, current formulations generally assert that the resistance of a process zone formed under static loading is maintained in the transition to fatigue loading.

Few validation tests that address delamination in composite materials with large process zones under complex loading conditions are available in the literature. Carreras et al. presented a test [42] that considers the 3D effects of a structure for mode I fatigue delamination based on a reinforced DCB specimen (R-DCB) made of glass fiber that exhibited large-scale fiber bridging. Jensen et al. investigated delamination under fatigue loading applied by blocks of different amplitude [43]. An analysis of the transient delamination growth under variable amplitude loading in G-control [44] was performed by the same authors. However the previous works were limited to mode I. To the author's best knowledge, the only validation test that investigates the contribution of the $\mathcal{R}$-curve effects in complex structures and loading conditions (mode I, II and III), considering the loading history, is the one presented in [45].

This article focuses on evaluating whether the state-of-the-art CZM-related tools are able to model delamination in complex structures accurately, considering the $\mathcal{R}$-curve effects and loading history, and under static and fatigue loading conditions. To this end, the capabilities and limitations of a CZM-based simulation strategy built with state-of-the-art methods are evaluated by simulating the validation benchmark test presented in [45]. In addition, insights into the relationship between the features of the simulation strategy and the physics of the delamination process are thoroughly discussed.

The structure of the document is as follows: Section 2 proposes a modeling and simulation methodology based on state-of-the-art CZM-related techniques that have the potential to predict delamination in complex composite structures considering large process zones and loading history under static and fatigue loading. Section 3 describes the modeling of the validation benchmark test used as a case study to evaluate the capabilities of the modeling strategy. In Section 4, the results of the benchmark simulation are presented and compared against the experimental results presented in [45]. The results are discussed in Section 5, with a focus on analyzing the connection between the results and the underlying physics of the problem. Section 6 provides the conclusions.

2. Modeling and simulation methodology

The modeling and simulation (M&S) strategy for delamination undergoing large damage process zones under static and fatigue is presented in this section. The M&S strategy is based on a static cohesive zone model that considers the loading mode mixity [12], a fatigue CZM able to model fatigue onset and propagation resistance [35], and a superposition strategy to model large fracture process zones [2,13,38,46]. The cohesive law parameters are extracted from experimental loading–displacement curves following the procedures described in [47,48], and the $\mathcal{R}$-curve of the material is considered by superposing several cohesive zone laws, such as in [38]. The fatigue parameters are experimentally determined from fatigue onset and propagation fracture tests following the fatigue parameter determination method presented in [37]. To consider the fatigue $\mathcal{R}$-curve effects, fatigue damage was allowed to be accumulated independently in each superimposed cohesive law as proposed in [46].

2.1. Static formulation

The static cohesive zone model (CZM) [12] comprises a bi-linear traction–displacement jump law designed to address mixed-mode loading conditions (see Fig. 1a). In this model, the mixed-mode equivalent traction (τ) is defined as a function of the mixed-mode equivalent displacement jump (λ):

$$\tau = (1 - d)\, K_B \lambda \tag{1}$$

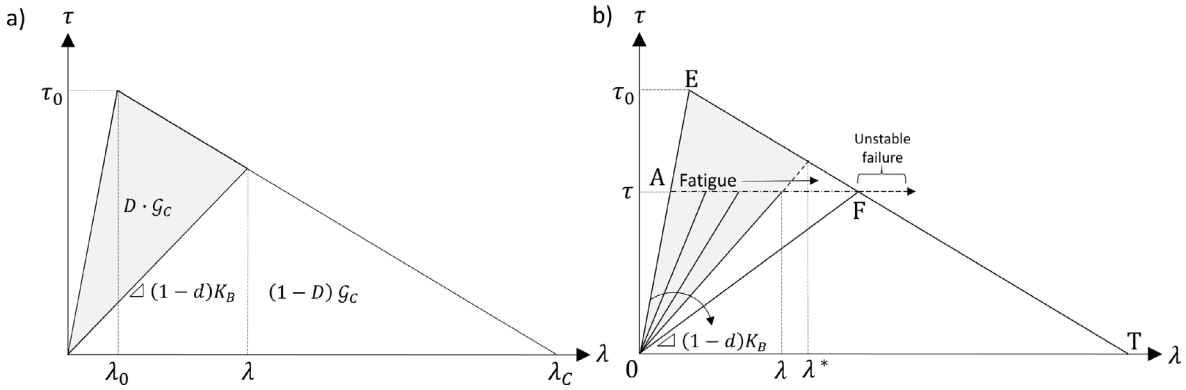

Fig. 1. (a) Representation of the bilinear constitutive law used in the formulation for a fixed mode ratio (b) Fatigue damage accumulation under subcritical traction.

where d is the stiffness damage variable, λ is the displacements jump norm, K_B is a mode-dependent penalty stiffness:

$$K_B = K_{33}(1 - B) + BK_{sh} \tag{2}$$

and B is the local mixed-mode ratio, which is a function of the pure mode displacement jump state and penalty stiffness:

$$B = \frac{K_{11}\Delta_1^2 + K_{22}\Delta_2^2}{K_{11}\Delta_1^2 + K_{22}\Delta_2^2 + K_{33}\langle\Delta_3\rangle^2} \tag{3}$$

having the following relationship between the penalty stiffness: $k_{11} = k_{22} = k_{sh}$, and being λ_i the pure mode displacement jump. The subscript (.)3 refers to the opening direction, while (.)1 and (.)2 are orthogonal shear directions. When the loading mode conditions are changed, the value of the stiffness damage variable, d, is kept fixed while the fracture toughness and the penalty stiffness are interpolated as a function of the local mixed-mode ratio, B. Further details of the formulation can be found in [12].

2.2. Cohesive law parameter determination accounting for R-curve effects under static loading

A simple bi-linear cohesive law can effectively predict crack propagation in quasi-brittle materials. However, when materials exhibit $\mathcal{R}$-curve behavior involving multiple damage mechanisms, more complex CL shapes are needed, which can be defined by a series of bi-linear cohesive laws (CL) that can be superimposed to model the delamination behavior. This approach accounts for the influence of distinct damage mechanisms without using more complex cohesive laws, as discussed in [38] and implemented in [13]. If these superimposed cohesive laws are integrated, the resulting cohesive law envelope represents the material's $\mathcal{R}$-curve. To define the cohesive law envelope, an inverse data reduction method that relies on experimental static load–displacement curves is used. The parameters for each superimposed cohesive law are determined through an iterative process to fit the cohesive envelope [47,48].

2.3. Fatigue formulation

The fatigue cohesive zone model (FCZM) from [35] is used to model fatigue degradation. The formulation assumes that the static cohesive law essentially serves as the envelope for fatigue damage. Given a single material point subjected to a sub-critical constant load scenario, damage accumulates due to cyclic loading (Fig. 1b, progressing horizontally in a sub-critical way from point A to F). Once point F is reached, the material point fails catastrophically due to its inability to bear the load. This could be the case of an S–N characterization test. However, if there are other material points in the damage process zone at a lower sub-critical loading level (e.g. a crack propagation in a DCB specimen), a stress redistribution would be produced, allowing the stress at the given material point to follow the decreasing branch of the cohesive law (F to T). The local displacement jump, λ, which uses concepts of the S–N curves, determines the fatigue damage rate accumulation function:

$$\frac{dD}{dN} = \frac{1}{\gamma}\frac{(1 - D)^{\beta - p}}{E^{\beta}(p + 1)}\left(\frac{\lambda}{\lambda^*}\right)^{\beta} \tag{4}$$

where D is the energy damage variable, λ^* is the equivalent displacement jump that would onset static tearing, and γ is the number of cycles at which infinite life is considered. p is a non-dimensional material-dependent coefficient that does not affect the S–N curve definition [49], nevertheless, it has an impact on the Paris' law coefficient C and in the low cycle fatigue resistance. β is the slope of the S–N curve defined by:

$$\beta = \frac{-7\eta}{log\ E} \tag{5}$$

The parameter η represents brittleness and accommodates the upward curvature of certain materials in their low cycle fatigue behavior. E is the endurance limit at a given stress ratio R and mode-mixity B. In the original formulation of the fatigue CZM [35], E was related to the relative endurance ε ($R = -1$, B=0) by the Goodman relation:

$$E = \frac{2C_L\varepsilon}{C_L\varepsilon + 1 + (C_L\varepsilon - 1)\,R} \tag{6}$$

where $C_L = 1 - 0.42\ B$.

The energy damage variable D, which acts as the internal variable of the damage model, and the stiffness damage variable d are linked as detailed in [12]. Further details of the fatigue formulation can be found in [35].

In addition, a load envelope strategy is implemented to enhance the efficiency of fatigue crack growth calculations. This strategy involves the calculation of the cycle jump per iteration, ΔN:

$$\Delta N = \frac{\Delta D_{\max}}{\max\limits_{j\in CZ}\left\{\frac{\partial D_{\mathrm{fat},j.}}{\partial N}\right\}} \tag{7}$$

where $\Delta D_{\max}$ is the maximum damage increment allowed by the user and $\max\limits_{j\in CZ}\left\{\frac{\partial D_{\mathrm{fat},j.}}{\partial N}\right\}$ represents the highest fatigue damage rate among all integration points, denoted as j, that experience damage within the cohesive zone (CZ) in the previous iteration. This approach ensures that no material point exceeds the maximum permissible damage increment in a given iteration.

2.4. Fatigue parameter determination considering fatigue R-curve effects

A fatigue parameter architecture, enabling the accumulation of fatigue damage at different rates within superimposed cohesive laws is essential for accurately replicating the experimentally measured $\mathcal{R}$-curve effects in fatigue onset and propagation. The developed approach aims to imitate how various damage mechanisms in the process zone accumulate fatigue damage to reproduce the physical behavior accurately.

Table 1
Fatigue law superposition architecture to model the $\mathcal{R}$-curve effects.

Fatigue parameter	FCL1	FCL2	FCL3	FCL4	FCL5
ε	ε	ε	ε	–	–
p	p	p	p	–	–
η	1	η_A	η_B	–	–

The fatigue formulation relies on three parameters (ε, p, and η) that define the fatigue behavior of each superimposed cohesive laws. To strike a balance between modeling precision and parameter determination, the fatigue damage accumulation architecture outlined in [46] is adopted. This approach involves a multi-step process. Fatigue damage is disabled for cohesive laws representing the toughening effects of low-density long fiber bridging [50]. This modeling choice is adopted based on the best fit of characterization data performed in [46]. It is assumed that, under sub-critical loading conditions, the fatigue dissipation energy associated with these cohesive laws is negligible. To encapsulate the combined impact of various concurrent failure mechanisms, the parameters ε and p have the same value for the rest of the superimposed cohesive laws. The brittleness parameter (η) is individually adjusted for each cohesive law in which fatigue damage accumulation is activated, capturing the variations in fatigue damage rates that the different failure modes might have. Notably, the brittleness parameter (η) is consistently set to 1 in the cohesive law with higher static strength, symbolizing the quasi-brittle fracture of the matrix [38,51]

Table 1 shows an example of the proposed architecture applied to a cohesive law superposition using 5 cohesive laws. As it is stated in the previous paragraph, since the fatigue parameters for CL4 and CL5 represent the fatigue energy dissipation related to fiber bridging, no fatigue damage is activated [46]. The rest of the superimposed cohesive laws (CL1–CL3) have the same values for the ε and p parameters. Parameter η is determined independently for the remaining CL, except for the cohesive law with higher static strength (CL1), where η is set to 1. Therefore, the fatigue parameters that must be determined with this architecture are: ε, p, η_A, and η_B

The methodology presented in [37] is used here to determine the fatigue parameters by comparing the onset and propagation data from the fatigue tests, against the output of the model.

3. Case study definition

A benchmark test [45], which considers the contribution of large process zones and the load history, is used as a case study to evaluate the capabilities of the $M\&S$ strategy presented in this paper. The details of the benchmark test are explained first, followed by the $M\&S$ strategy for its simulation.

3.1. Benchmark test definition

The hybrid static-fatigue benchmark test applied to a specimen with a material exhibiting a large process zone [45] is selected. The benchmark tests employ beam-like specimens as those used in standardized DCB or ELS characterization tests, with the particularity that the loading blocks are not perpendicular to the longitudinal direction of the specimen (Fig. 2). The material of the specimen was Solvay's APC (PEKK-FC) thermoplastic polymer prepreg, featuring a fast-crystallizing thermoplastic matrix (PEKK-FC) reinforced with continuous unidirectional AS4D carbon fibers, each with a nominal ply thickness of 0.138 mm. The specimens were designed to be 25 mm wide, 225 mm long, and approximately 4.2 mm thick. Due to the high melting temperature of thermoplastic composites, a 12.5 μm-thick UPILEX foil (60 mm long) was used as an insert to initiate the crack.

The experimental test was designed to induce a varied crack front shape by rotating the loading blocks. The loading fixtures were oriented

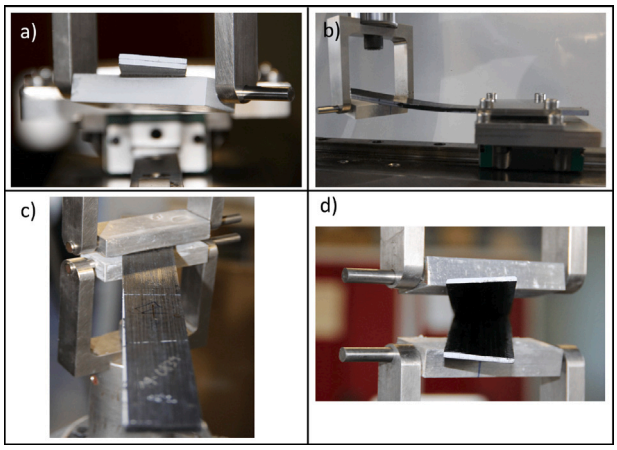

Fig. 2. (a) front and (b) lateral photographs of shear mode loading in the ELS test rig, and (c) top and (d) front photographs of the Mode I loading in the DCB test rig with the loading block inclined with respect to the longitudinal direction of the specimen.

Table 2
Boundary conditions of each step in the hybrid static-fatigue test simulation.

Step	Loading mode	Loading angle, α [°]	Maximum displacement, δ_{max} [mm]	Number of cycles
H.1	Mode I	+ 0°	12.5	- (static)
H.2	Shear mode	+ 30°	7	12 000
H.3a	Mode I	−30°	5	30 000
H.3b	Mode I	−30°	10	- (static)
H.3c	Mode I	−30°	10	400 000

at an angle (α) with respect to the specimen transversal section, imposing a SERR gradient along the delamination front (refer to Fig. 3). Consequently, the delamination front shape evolved differently along the specimen's longitudinal direction as the delamination progressed. X-ray tomography was used to monitor the delamination process evolution. An automated procedure was developed to post-process the X-ray images, aiming at detecting both the delamination leading front and the wake of the damage process zone (FPZ). Various loading conditions, including static and fatigue loading, under multiple loading modes, were applied during the test. The loading sequence, outlined in Table 2, was as follows:

1. Step H.1: The benchmark test started from the insert at an initial crack length a_0 of 41 mm. A mode I static pre-crack of δ_{max} = 15 mm was performed, with the loading block set perpendicular to the longitudinal direction of the specimen (α = 0, Fig. 3a). The objective was to create a leading delamination front perpendicular to the longitudinal direction of the specimen with a developed static damage process zone in the wake.
2. Step H.2: Shear mode fatigue loading was applied with the ELS test rig, but setting the loading block inclined + α in a counter-clockwise direction with respect to the longitudinal direction of the delamination plane (Fig. 3b). The specimen length l from the most distant point of the loading block to the clamping fixture was set to 90 mm, and the distance to the pre-crack, a_0, of 56 mm. This configuration underwent loading for 12k cycles.
3. Step H.3: A mode I DCB was applied to the existing shear mode leading delamination front. The loading block angle was inverted from + α to − α by pure rotation of the loading blocks with respect to the middle point of the specimen width (clockwise direction) (Fig. 3c). First, step H.3a, a fatigue loading with a maximum applied displacement of 5 mm was applied for 30k cycles. Then, step H.3b, a static loading up to an opening of 10 mm was imposed on the existing delamination process. Finally, step H.3c, 400k cycles of 10 mm maximum displacement were applied.

Table 3
Details of the Finite Element model of the validation benchmark test.

Parameter	–
l: Length of the specimen	118.6 mm
w: Width of the specimen	25 mm
t: Arm thickness	2.1 mm
l_{clamp}: Clamping compliance correction	28.6 mm
a_0: initial crack length	41 mm
l_e: Cohesive element length	0.2 mm
Elements in sub-laminate thickness	8
Element type in beams	SC8R (Abaqus 6.14-2)
Δd_t: Fatigue damage target per iteration	2E−2
Solver	Implicit, Newton – Raphson, NLGEOM static
Cohesive element	COH3D8 + UMAT subroutine

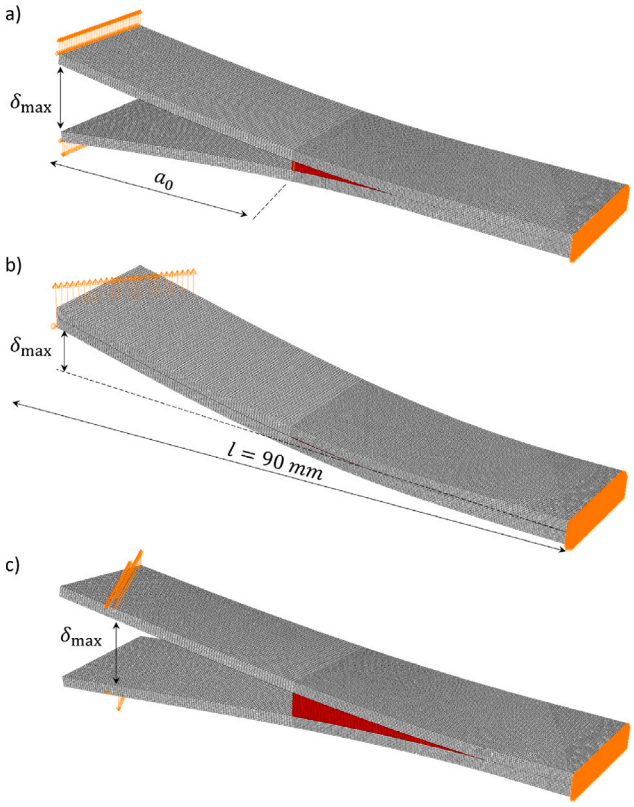

Fig. 3. Schematic representation of the characterization models: (a) Step H.1: static pre-crack with DCB configuration, (b) Step H.2: ELS configuration with + 30° inclination of the imposed displacement, and (c) Step H.3: DCB configuration with −30° inclination of the imposed displacement.

Note that the displacement ratio in the fatigue loading steps was $R_d = \delta_{min}/\delta_{max} = 0.1$. The delamination process was monitored by X-ray radiography, locating the delamination leading tip and the wake of the process zone [45]. Fig. 4a–d presents an overview of the delamination process evolution, where the most significant events of each step are summarized. In Fig. 4e, a graphical representation of the fracture surfaces created under each load step is represented, where H.1 and H.3 are mode I fracture surfaces, and H.2 the shear mode fracture surface.

3.2. Modeling and simulation strategy implemented for the case study

An ABAQUS finite element model of the benchmark specimen was developed. SC8R continuum shell elements modeled the specimen arms, while COH3D8 interface elements were used to represent the interface between the upper and lower arms. The specimen arms were modeled as linear elastic, and the cohesive zone model described in Section 2 was implemented in a UMAT user-written subroutine. The details of the finite element model are summarized in Table 3.

Table 4
AS4D/PEKK-FC thermoplastic composite elastic properties at room temperature [2].

Property	Description	Value	Unit
E_{1t}	Young's modulus, fiber tensile direction	138 300	MPa
E_{2t}	Young's modulus, matrix tensile direction	10 400	MPa
$G_{12} = G_{13}$	Shear modulus	5190	MPa
ν_{12}	Poisson ratio, 1–2 direction	0.316	–
ν_{23}	Poisson ratio, 2–3 direction	0.487	–

The boundary condition sequence used for the benchmark test simulation is outlined in Table 2, and the boundary conditions for different load steps are illustrated in Fig. 3.

The elastic properties of the laminate are summarized in Table 4. The interlaminar static fracture properties were characterized in [52], the fatigue mode I properties in [46], and the mode II properties in [53] (Table 5).

3.2.1. Static and fatigue cohesive law parameters

As discussed in [52], the nonlinear softening behavior of this material is represented by the superposition of five bi-linear cohesive laws. This cohesive envelope captures the material's static delamination resistance, accounting for the large process zone. Subsequently, the fatigue behavior is determined, accumulating fatigue damage within this cohesive envelope.

The cohesive law envelope for mode I and shear mode loading was established in [2] following the methodology developed in [47,48]. The $\mathcal{R}$-curve, determined from static tests in [2], serves as a representation of delamination resistance concerning the large process zone. Through an iterative process, the superimposed cohesive laws that define the cohesive envelope were determined to accurately fit the experimental $\mathcal{R}$-curve of the material. The parameters defining each cohesive law are provided in Table 6, including the total energy dissipated at the complete damage of each cohesive law as a function of the loading mode. The shear mode properties were set to be equal in all directions, making no distinctions between mode II and mode III.

Note that CL5 under shear loading mode does not significantly contribute to the shear mode $\mathcal{R}$-curve, because it dissipates only 1E-4 N/mm when fully damaged. This implies that the representation of the shear mode $\mathcal{R}$-curve requires only four superimposed cohesive laws. Therefore, due to numerical reasons, the CL5 critical opening under shear mode loading ($\lambda_{C,shear}$) was adjusted to match the critical opening of CL4. Therefore, under shear mode loading, the specific energy dissipation isolines of CL5 and CL4 propagate together at the same critical opening value.

The $\mathcal{R}$-curve for both mode I and shear mode loading, derived from the superposition of cohesive laws, is illustrated in Figs. 5a and 5b. The dashed lines in the figures represent the total energy dissipated at the complete damage of each cohesive law. These curves demonstrate the development of the $\mathcal{R}$-curve as the superimposed cohesive laws undergo damage.

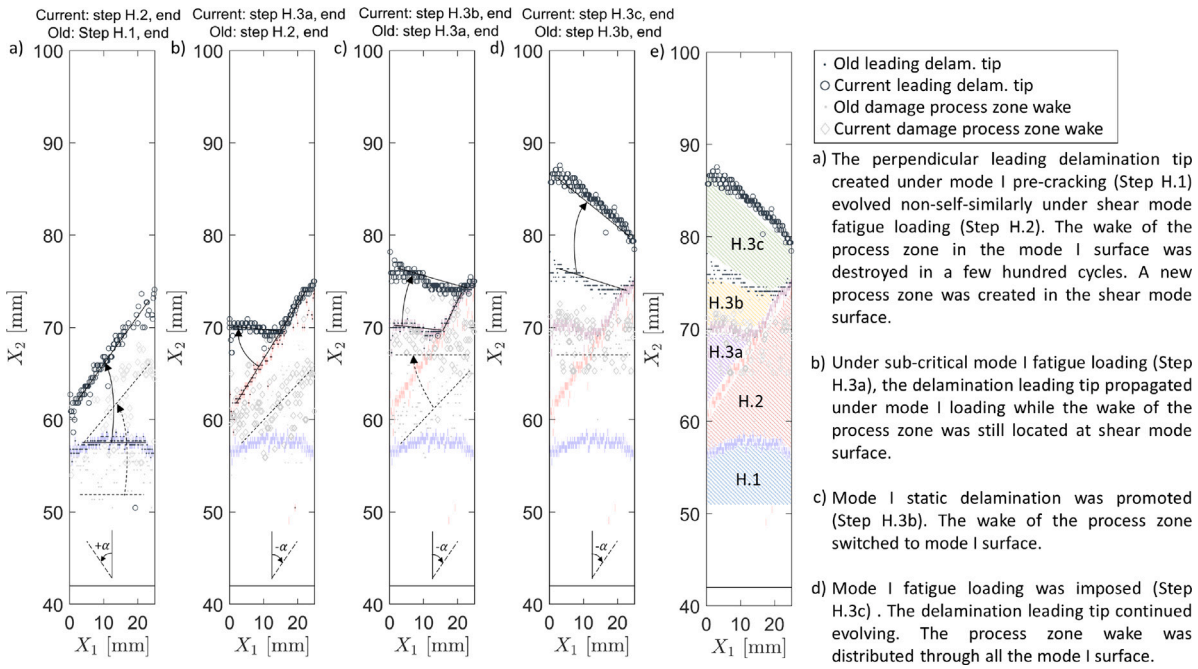

Fig. 4. Overview of the fatigue benchmark results (a–d). Graphical representation of the fracture surfaces created under each load step (e), where H1 and H3 are mode I fracture surfaces, and H2 is shear mode fracture surface.
Source: Adapted from [45].

Table 5
AS4D/PEKK-FC thermoplastic composite fracture properties at room temperature [46,52].

Property	Description	Procedure	Value	Unit
$\mathcal{G}_{\mathrm{Ic},i}$	Mode I fracture toughness, initiation	ASTMD 5528 [2,54]	0.7	N/mm
$\mathcal{G}_{\mathrm{Ic},p}$	Mode I fracture toughness, propagation	ASTMD 5528 [2,54]	1.12	N/mm
$\mathcal{G}_{\mathrm{IIc},i}$	Mode II fracture toughness, initiation	ISO 15114 [2,55]	1.45	N/mm
$\mathcal{G}_{\mathrm{IIc},p}$	Mode II fracture toughness, propagation	ISO 15114 [2,55]	2.35	N/mm
C_{I}	Mode I Paris' law coefficient	Multi-fatigue test rig [46]	93.2	mm/cycle
p_{I}	Mode I Paris' law exponent	Multi-fatigue test rig [46]	8.87	–
C_{II}	Mode II Paris' law coefficient	Multi-fatigue test rig [53]	3.82E−2	mm/cycle
p_{II}	Mode II Paris' law exponent	Multi-fatigue test rig [53]	2.87	–

Table 6
Definition of the superimposed static cohesive laws (CL) and total energy dissipated at complete damage of each superimposed cohesive law.

	CL1	CL2	CL3	CL4	CL5
k_{I}: Mode I penalty stiffness [N/mm^3]	1E6	4.5E5	9.17E4	1.67E4	3.33E3
$\tau_{0,\mathrm{I}}$: Mode I strength [MPa]	62	20	5.5	0.5	0.2
$\mathcal{G}_{\mathrm{IC}}$: Mode I fracture toughness [N/mm]	0.28	0.25	0.25	0.1	0.24
$\tau_{0,\mathrm{shear}}$: Shear mode strength [MPa]	28	22	10	0.1	1E−4
$\mathcal{G}_{C,\mathrm{shear}}$: Shear mode fracture toughness [N/mm]	0.6	1.2	0.45	0.1	1E−4
Total energy dissipated under mode I loading [N/mm]	0.48	0.67	0.84	0.95	1.12
Total energy dissipated under shear mode loading [N/mm]	1.69	2.22	2.26	2.35	2.35

For the later interpretation of the results, Fig. 5c represents a delamination state of a simple mode I DCB test considering non-negligible process zone, while Fig. 5d represents the delamination under shear mode loading. Each of the colored lines represents the complete damage of a superimposed cohesive law and gives a measure of the $\mathcal{R}$-curve development within the process zone in terms of dissipated energy. The gray crosses are the numerical delamination leading tip and represent the start of the process zone, being the 0 N/mm specific energy dissipated isoline. The remaining specific energy-dissipated isolines represent the total damage of superimposed cohesive laws CL1 to CL5. They are associated with the fracture toughness of each cohesive law as defined in Table 6. These results provide a measure of the total energy dissipated as a function of the location within the process zone. The results can be interpreted as specific energy dissipation ($\mathcal{G}$) isolines that define the evolution of the material's $\mathcal{R}$-curve.

After completing the static characterization, the parameters for the fatigue degradation of each cohesive law are determined. The method, described in Section 2 and based on the developments presented in [37], incorporates the experimental data from [46] and mode II properties from [53] to obtain the parameters of the fatigue model. These parameters are summarized in Table 7.

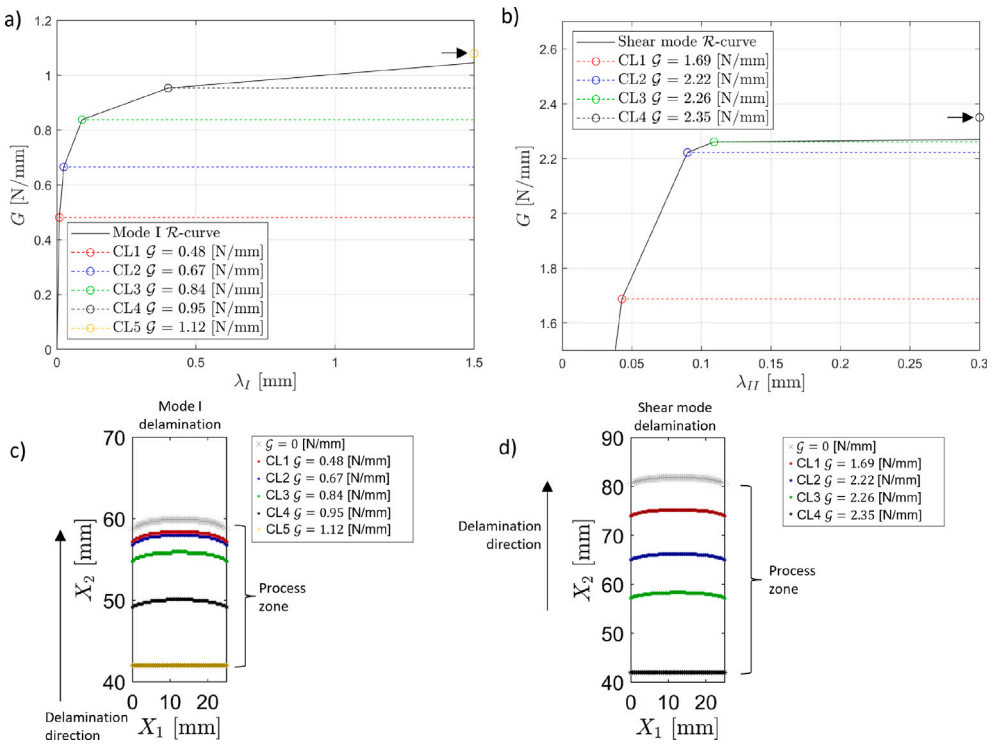

Fig. 5. Numerical modeling of the $\mathcal{R}$-curve, where the dashed lines represent the energy dissipated when each superimposed cohesive law is completely damaged under (a) mode loading I, and (b) shear mode loading. Examples of numerical process zone result representation on DCB specimens for (c) mode I and (d) shear mode loading. Each line represents a fully damaged cohesive law and gives a measure of the $\mathcal{R}$-curve development state.

Table 7
Obtained fatigue parameters considering fatigue onset and propagation data:

ε [−]	p [−]	η_A [−]	η_B [−]	γ_1 [−]	γ_{shear} [−]
0.0402	β − 2.14	0.907	0.689	1E6	1.6E5

4. Results

In this section, the predicted evolution of the delamination process is compared against the experimental results presented in [45]. In the experimental data, the delamination process is confined by the delamination leading front and the damage process zone wake, which are measured by X-ray tomography. In the numerical predictions, specific dissipated energy isolines are plotted to represent the development of the $\mathcal{R}$-curve within the damage process zone. To do so, the complete damage of each of the superimposed cohesive laws is visualized, which can be correlated to the amount of specific dissipated energy as illustrated in Fig. 5, where the colored isolines represent the energy dissipated when each superimposed cohesive law is completely damaged.

4.1. Step H.1: Static mode I loading, + 0° loading angle

In the H.1 step (Table 2), a static mode I delamination was performed with the applied load perpendicular to the delamination direction (Fig. 3a). The delamination process started from the insert at an initial crack length a_0 of 41 mm. As the delamination advanced, a mode I process zone was formed, developing the mode I $\mathcal{R}$-curve along the cohesive zone (region constrained by CL1 and CL5 $\mathcal{G}$ isolines). As it can be seen in Fig. 6, at the end of Step H.1, the numerical delamination leading front ($\mathcal{G}$ = 0 N/mm), propagated about 5 mm more than the experimentally detected leading delamination front (gray stars). A physics-based explanation of this difference is made in the 5.1 discussion section. The experimental leading delamination front falled between CL1 and CL2 $\mathcal{G}$ isolines. Experimental process zone wake events (gray crosses) lay between CL3 and CL4 $\mathcal{G}$ isolines. And CL5 $\mathcal{G}$ isoline did not start to propagate and remained in the insert position.

4.2. Step H.2: Fatigue shear mode loading, + 30° loading angle

After the H.1 pre-cracking step, the boundary conditions were changed. The displacement was applied at an angle α = +30° in an ELS test configuration (Fig. 3b, Table 2). This rotation positioned the furthest point of the loading block at a distance of 56 mm from the former delamination front. During the H.2 step, fatigue shear mode was imposed with a maximum displacement of 7 mm and displacement ratio R = 0.1, having sub-critical shear mode loading. As the loading mode changed from pure mode I to pure shear mode, the energy available within the cohesive zone was interpolated from mode I to shear mode configuration (Fig. 6, Legend step H.1 to Legend step H.2).

The numerical leading delamination front ($\mathcal{G}$ = 0 N/mm) propagated about 10 mm ahead of the experimental observations. A physics-based explanation of this difference is made in 5.2 discussion section. The CL1 $\mathcal{G}$ isoline correlates with the experimental leading delamination front. CL2 and CL3 $\mathcal{G}$ isolines (Fig. 6, N = 1000–12000) correlate with the onset of the shear mode process zone, experimentally measured by the detection of the process zone wake. In contrast, the CL4 isoline did not propagate. As a result, the numerical model predicted that the process zone that was created under mode I loading (the region between CL3 and CL4 isolines) almost did not evolve under shear mode loading. Only after 10k cycles, the CL3 isoline started to move from the right-hand side.

4.3. Step H.3a: Fatigue mode I loading, −30° loading angle

In step H.3a (Table 2), the boundary conditions were changed to a mode I configuration, and the loading line angle was rotated from + 30°

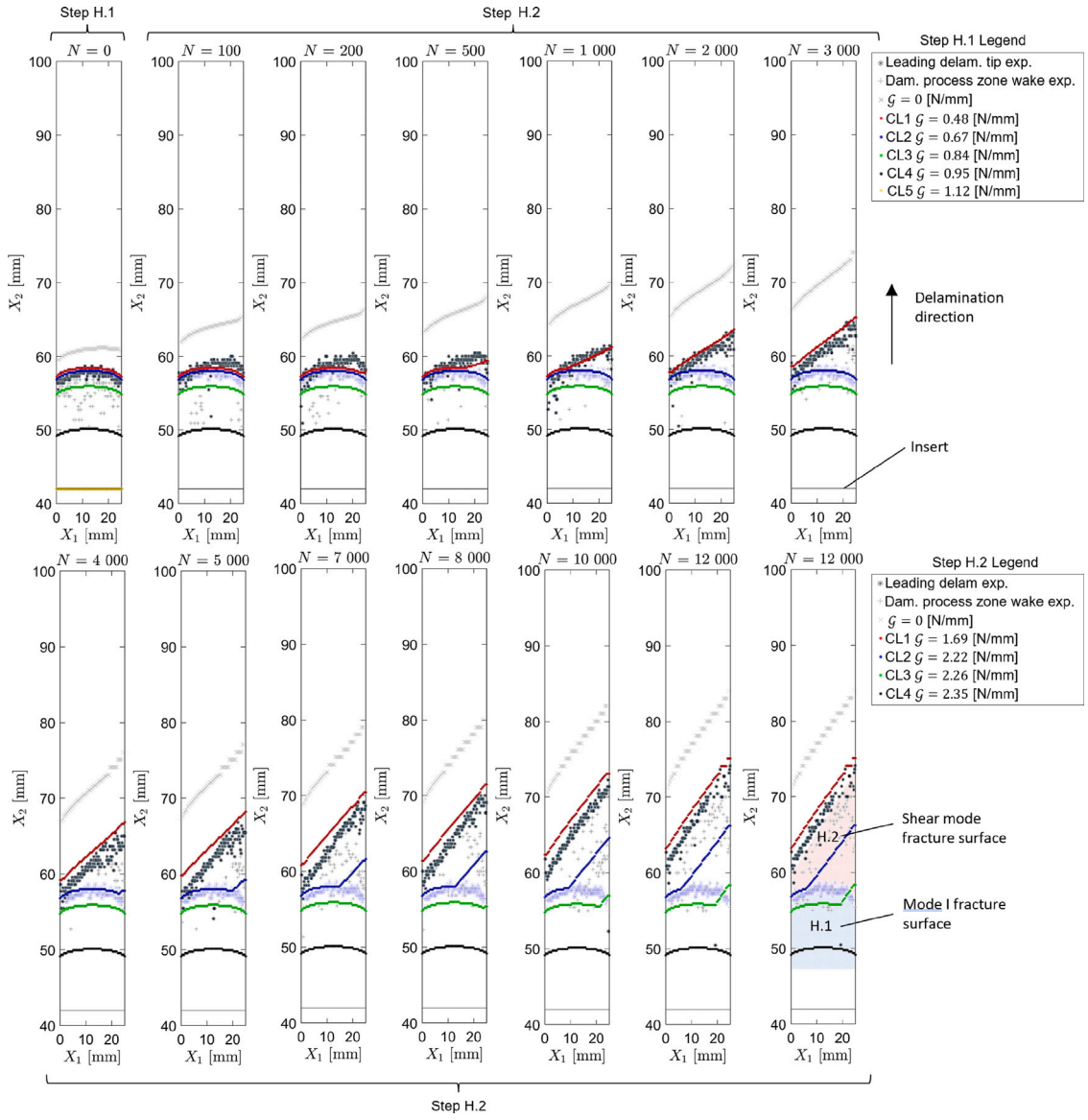

Fig. 6. Representation of the numerically predicted delamination process evolution compared over the experimental results presented in [45] for validation test step H.1 and H.2.

to −30° (Fig. 3c). A maximum displacement of 5 mm and R=0.1 was imposed, resulting in a sub-critical fatigue loading. The superimposed cohesive laws were automatically interpolated again to pure mode I properties. The maximum fatigue displacement of 5 mm caused the CL2 to CL4 $\mathcal{G}$ isolines to statically propagate. At the start of the fatigue loading, $N = 100$, the CL1 $\mathcal{G}$ isoline correlated with the experimental leading delamination front, and the experimental damage process zone wake was detected between CL2 and CL3 $\mathcal{G}$ isolines. However, the CL4 and CL5 $\mathcal{G}$ isolines were located in the static mode I pre-crack zone, where no experimental evidence of a process zone was found. During the first 30 000 cycles, the numerical $\mathcal{G}$ isolines did almost not propagate, underpredicting the fatigue delamination propagation (see Fig. 7).

4.4. Step H.3b: Static mode I loading, −30° loading angle

After the sub-critical mode I fatigue (Table 2), the maximum displacement was statically increased from 5 mm to 10 mm. After the static loading, the delamination process is plotted in Fig. 8, $N = 0$. All the numerical $\mathcal{G}$ isolines propagated due to the static loading, except the CL5 $\mathcal{G}$ isoline. Note that under Mode I loading conditions, since the critical opening of CL5 is greater than the critical opening of CL4, and the fatigue damage is deactivated at both CL4 and CL5, the damage propagation at both cohesive laws is governed by the static stress redistribution on the specimen as the fatigue damage propagates at CL1, CL2, and CL3. As can be seen in Fig. 8, this stress redistribution propagates the specific energy dissipation isoline of CL4, but not that of CL5. This is because the openings at CL5 do not reach the critical opening value. The predicted delamination front location was short with respect to the experimental measurements. A maximum mismatch of 10 mm between CL1 $\mathcal{G}$ isoline and the experimental leading front was found after step H.3a. However, the experimental detection of the process zone wake correlated between CL2 and CL3. CL4 was located in the shear mode surface, where no experimental process zone wake was experimentally detected.

4.5. Step H.3c: Fatigue mode I loading, −30° loading angle

Finally, mode I fatigue with $d_{max} = 10$ mm and $R = 0.1$ was applied (Table 2). During the first 5000 cycles, a transient behavior was observed, where the numerical $\mathcal{G}$ isolines propagate faster than the experimentally determined leading delamination front results. This

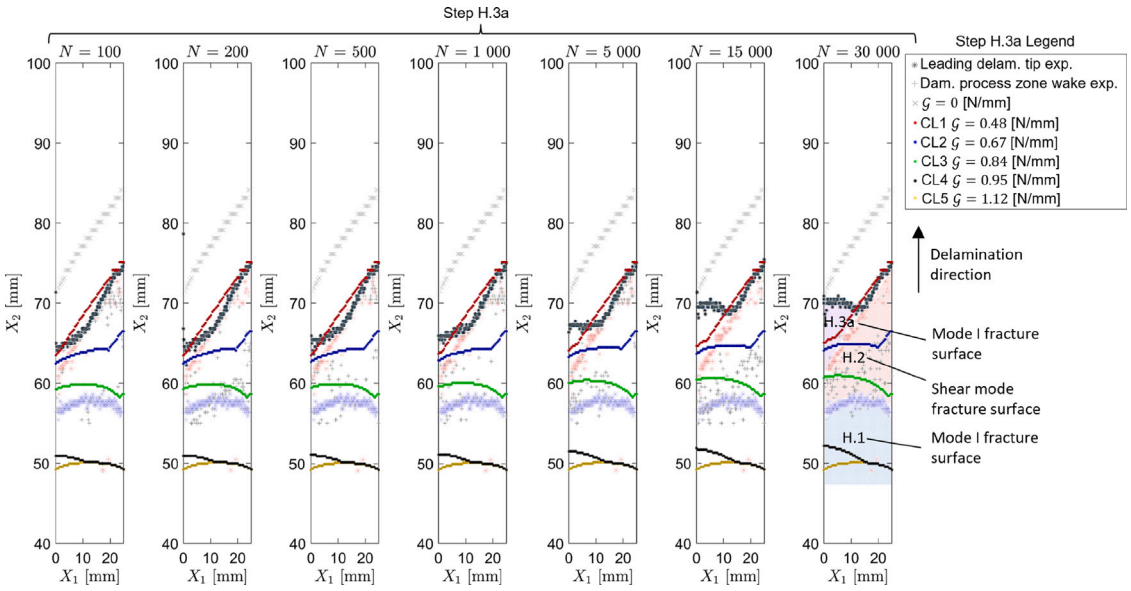

Fig. 7. Representation of the numerically predicted delamination process evolution compared over the experimental results presented in [45] for validation test step H.3a.

trend ended when CL1 $\mathcal{G}$ isoline accurately correlated again with the experimental leading delamination front. The experimental wake of the process zone did not propagate during the fatigue loading. However, the numerical process zone did, showing the evolution of the $\mathcal{R}$-curve. For the first 1000 cycles, the experimental process zone wake correlated with the CL3 $\mathcal{G}$ isoline, between cycles 5000 and 100 000 with the CL4 $\mathcal{G}$ isoline, and from that point on, with the CL5 $\mathcal{G}$ isoline, which did not propagate during the whole fatigue loading.

5. Discussion

In this section, the results obtained with the *M&S* approach followed in this study are discussed. Moreover, the numerical results obtained complement some of the experimental findings of [45] on how failure mechanisms vary with test boundary conditions in non-self-similar delamination processes presented.

5.1. Physical significance of modeling the R-curve development with superimposed cohesive laws under static loading

The numerical evolution of the $\mathcal{R}$-curve within the cohesive zone in step H.1 was compared with the X-ray monitoring of the delamination process evolution. The experimental leading delamination front location correlated between the CL1 and CL2 isolines (0.48 and 0.67 N/mm), aligning with the fracture toughness onset characterized in the static DCB experiments presented in [2] ($\mathcal{G}_{\mathrm{Ic},i}$ = 0.7 N/mm, Table 5). Additionally, the wake of the damage process zone was experimentally located between the 0.67 and the 1.12 N/mm dissipated $\mathcal{G}$ isolines, correlating with the propagation fracture toughness, $\mathcal{G}_{\mathrm{Ic},p}$ = 1.12 N/mm, Table 5.

These results reinforce the assumption that each superimposed cohesive law represents a damage mechanism involved in the delamination process. Under mode I loading, the complete damage of CL1 (0.48 N/mm dissipated $\mathcal{G}$) maybe be correlated with quasi-brittle fracture. The complete damage of both CL1 and CL2, equivalent to 0.67 N/mm specific dissipated energy, could embody a combination of quasi-brittle fracture and the maximum plastic strain experienced by the matrix. Consequently, this leads to the complete failure of the matrix. This phenomenon explains why the CL1 and CL2 $\mathcal{G}$ isolines correlate with the experimental detection of the leading delamination front. The leading front is the point reached by the penetrating liquid during X-ray inspections, as detailed in the work by Leciñana et al. [45]. The other cohesive laws would represent the contribution of fiber bridging development.

5.2. Physical significance of modeling the R-curve development with superimposed cohesive laws under shear mode fatigue loading

In the case of the fatigue shear mode loading, the numerical damage onset was about 10 mm ahead of the experimental leading delamination front. This discrepancy may arise because, even if the matrix undergoes plastic strain and shear cusps form, there might be no continuity on the defects. As a result, the contrast liquid used in the X-ray inspections may not penetrate this region effectively. The CL1 $\mathcal{G}$ isoline (1.69 N/mm dissipated shear mode $\mathcal{G}$) correlated with the experimental leading delamination front location, which is close to the shear mode fracture toughness onset value $G_{\mathrm{IIc},i}$ = 1.45 N/mm, Table 5. The detection of the damage process zone wake correlates with CL2 and CL3 $\mathcal{G}$ isolines (2.22 and 2.26 N/mm dissipated shear mode $\mathcal{G}$), near the propagation fracture toughness value $G_{\mathrm{IIc},p}$ = 2.35 N/mm, Table 5. This observation may indicate the complete coalescence of the shear cusps. However, additional shear mode energy dissipation (up to 2.35 N/mm) lacks correlation to any experimental observation. This dissipation could be attributed to friction between the delaminated surfaces during the characterization test, rather than any damage mechanism, as discussed in [56].

5.3. Physical significance of modeling the R-curve development with superimposed cohesive laws under mode I fatigue loading

Regarding the fatigue mode I loading, after the transient state due to the shear mode cohesive zone effect was overcome (step H.3c, $N > 5000$ cycles), the complete damage of the CL1 and CL2 $\mathcal{G}$ isolines correlated with the experimental leading delamination front. As in shear mode loading, the numerical damage onset, 0 N/mm specific dissipation energy, was about 5 mm ahead of the experimental leading delamination front. This can be explained by assuming that in those 5 mm, a combination of quasi-brittle fracture and plastic deformation was undergoing in the thermoplastic matrix, and the contrast liquid used in the X-ray inspections could not penetrate inside this region of the material.

The evolution of the $\mathcal{R}$-curve, concurrent with the development of the process zone, can be linked to the correlation between the $\mathcal{G}$ isolines and the experimental wake of the process zone location. As the fatigue loading was applied, the experimental leading delamination front propagated while the experimental wake of the process zone did not, indicating the ongoing evolution of the process zone and

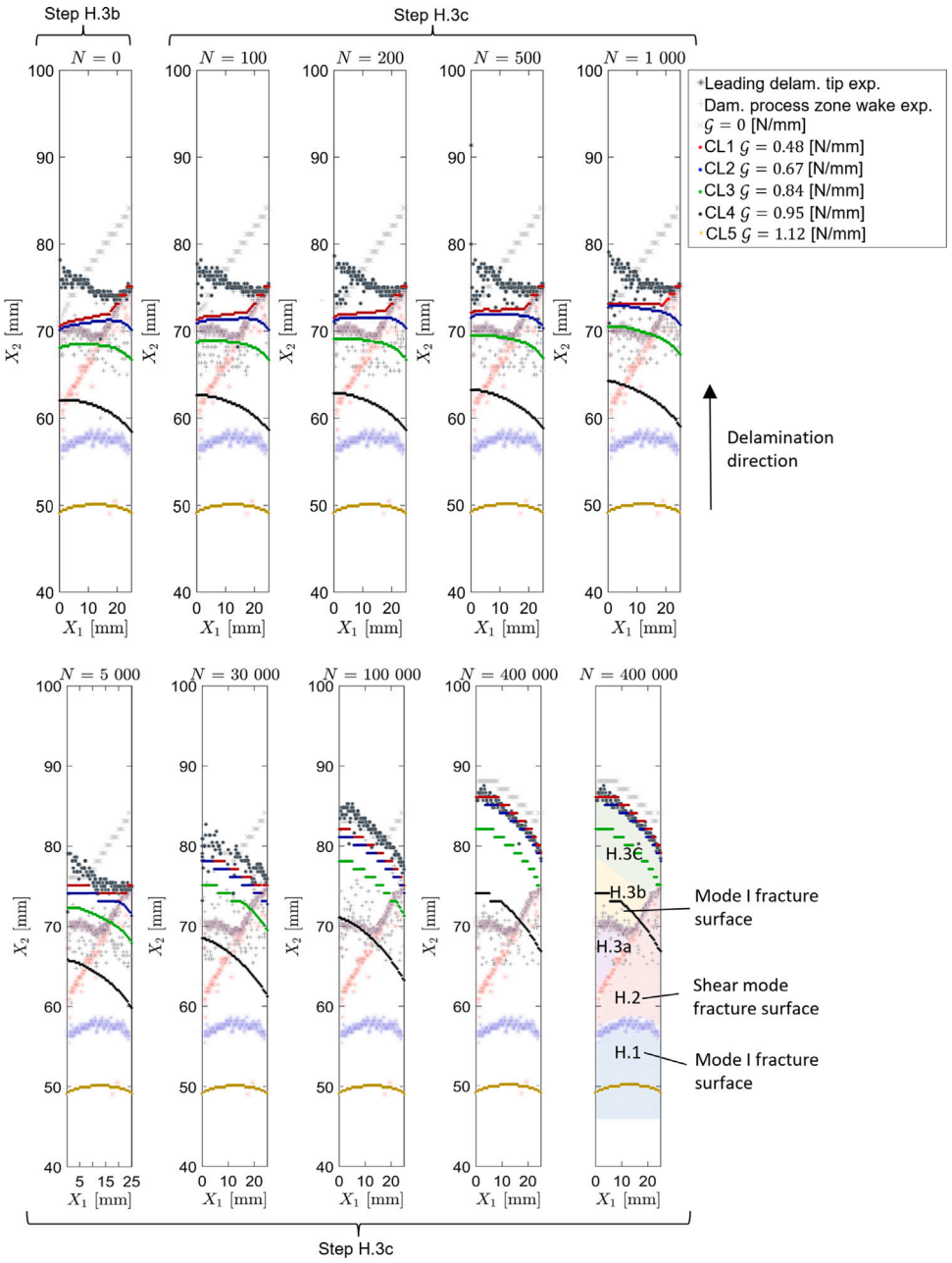

Fig. 8. Schematic representation of the characterization models: (a) static pre-crack with DCB configuration, (b) ELS configuration with + 30° inclination of the imposed displacement, and (c) DCB configuration with −30° inclination of the imposed displacement.

the development of the $\mathcal{R}$-curve. During the first 1000 cycles, the experimental process zone wake correlated with CL3 $\mathcal{G}$ isoline, between cycles 5000 and 100 000 with CL4 $\mathcal{G}$ isoline, and from that point onward, with the CL5 $\mathcal{G}$ isoline. This demonstrates the capability of the superimposed cohesive zone modeling to accurately capture the process zone evolution under fatigue loading.

5.4. Delamination modeling accuracy of the proposed modeling and simulation methodology

Overall, a good accuracy of the delamination predictions made with the proposed methodology in the blind simulation of the validation benchmark was obtained. In most cases, the arbitrarily shaped delamination front and the non-self-similar evolution of the damage process zone were well captured under static and fatigue loading. However, challenges arose in properly accounting for the contribution of a partially developed cohesive zone when transitioning between loading modes. While the superimposed cohesive law method effectively models the development of the material's $\mathcal{R}$-curve under unchanged loading mode conditions during cohesive zone evolution, it encounters difficulties when the loading mode changes in a developing cohesive zone. In such cases, the model interpolates this cohesive zone to an equivalently developed $\mathcal{R}$-curve state in the new loading mode. This behavior would be akin to a mode I process zone, where fiber bridging is developed, automatically transforming the fiber bridges into plastic ligaments when changing to shear mode loading—a physically infeasible scenario. It is worth noting that this problem is not unique to the proposed model and also occurs in mixed-mode interpolation models that consider the $\mathcal{R}$-curve of the material, as presented in [57–59]. As of the authors' knowledge cutoff, there is currently no model in the literature that effectively addresses this issue.

The authors find that research is needed to find a representative way to interpolate between loading modes considering the loading mode history. To achieve this purpose, the capability to resist delamination of a developed $\mathcal{R}$-curve after changing the loading mode must be experimentally quantified under both static and fatigue loading. To do so, a process zone should be developed under a certain loading mode, and then its fracture toughness should be measured under a different loading mode. This way, the $\mathcal{R}$-curve loading mode interpolation could be done considering the loading mode history.

The modeling inaccuracy had limited consequences on the precision of the predictions in the case of the shear mode fatigue delamination after the static mode I pre-crack (the cohesive zone created in step H.1). The large process zone created under mode I loading laid between CL3 and CL5 $\mathcal{G}$ isolines, contributing with a 0.45 N/mm fracture toughness (1.12 N/mm–0.67 N/mm), supposing a 40.2% of the total fracture toughness under mode I loading (0.45/1.12). However, when interpolating the cohesives laws to shear mode, the fracture toughness contribution between the CL3 and CL5 $\mathcal{G}$ isolines turned to only 0.13 N/mm (2.35 N/mm–2.22 N/mm), supposing a 5.5% of the total fracture toughness under shear mode loading (0.13/2.35). This indicates that the numerical process zone created under mode I loading has a nearly negligible contribution to shear mode delamination resistance, influenced by the distribution of fracture toughness among superimposed cohesive laws and the approach used for loading mode interpolation.

In contrast, the interpolation of the process zone developed under shear mode loading to mode I loading significantly affected the accuracy of delamination prediction under mode I loading. The process zone created under shear mode loading was confined between CL1 and CL4 $\mathcal{G}$ isolines. After the loading mode interpolation, the contribution of the process zone in mode I loading, in terms of fracture toughness, was 0.64 N/mm (1.12 N/mm–0.48 N/mm), accounting for 57.2% of the total fracture toughness under mode I loading (0.64/1.12).

Therefore, understanding the effectiveness of the contribution of the interpolated process zone under new loading conditions becomes crucial. With the employed mode interpolation method, the contribution of the previously formed cohesive zone is assumed to be as effective as if it had been developed under the new loading conditions.

These inaccuracies led to an under-prediction of the fatigue delamination propagation under sub-critical loading (step H.3a) and static mode I loading (step H.3b). However, this under-prediction was rectified during a transient state of fatigue loading in the first 5000 cycles of step H.3c. This correction was attributed to an increased fatigue damage accumulation rate resulting from the shorter delamination length. Once the interpolated cohesive zones were completely damaged, good correlation with the experimental data was reestablished.

6. Conclusions

This study evaluates the effectiveness of a cohesive zone modeling-based simulation strategy in fulfilling essential requirements for accurate delamination modeling in composite structures. The strategy considers large process zones ($\mathcal{R}$-curve) and loading mode history under both static and fatigue loading conditions. It encompasses a static cohesive zone model, accounting for loading mode mixity, and a fatigue cohesive zone model capable of simulating fatigue onset and propagation resistance. Static cohesive law parameters are obtained from experimental loading–displacement curves, incorporating the material's $\mathcal{R}$-curve through the superposition of multiple cohesive zone laws. Fatigue parameters are experimentally determined via fatigue onset and propagation fracture tests, employing the authors' developed fatigue parameter determination method. To consider fatigue $\mathcal{R}$-curve effects, fatigue damage accumulates independently in each superposed cohesive law.

The predictive capabilities of the model were assessed through blind simulation of a validation benchmark test deliberately designed to incorporate a non-self-similar delamination scenario under complex loading conditions. The boundary conditions were tailored to induce a delamination process evolution with a non-straight leading delamination front and a damage process zone that evolved under different loading mode conditions, including static and fatigue loading.

Overall, a good accuracy of the delamination predictions was obtained with the proposed methodology in the blind simulation of the validation benchmark test. In the majority of cases, the arbitrarily shaped delamination front and the non-self-similar evolution of the damage process zone were well captured under fatigue and static loading. Additionally, the study offered valuable insights into the relationship between the superposed cohesive laws and the underlying damage mechanisms in the delamination process:

- Under mode I loading, superposed cohesive laws CL1 and CL2 were associated with a combination of quasi-brittle fracture and maximum plastic strain experienced by the matrix. The correlation was made by considering the X-ray leading delamination front measurements and aligning the dissipated energy by these cohesive laws with the fracture toughness onset energy.
- The other mode I superposed cohesive laws were associated to fiber-bridging by considering the X-ray wake of the damage process zone detection and the propagation fracture toughness energy.
- Following the same observation criteria of mode I, under shear mode loading, the CL1 was associated to matrix plastic strain and shear cusps formation.
- The CL2 and CL3 laws under shear mode loading were correlated with the complete coalescence of the shear cusps.
- The CL4 could be attributed to the friction between the delaminated surfaces during the characterization test rather than being associated with any specific damage mechanism.

The model faced challenges in accurately representing the contribution of a developed cohesive zone when the loading mode changed. This limitation arises from the model's interpolation of an already developed process zone to an equivalently developed $\mathcal{R}$-curve state in the new loading mode, lacking physical meaning when modeling large process zones. This approach assumes that the contribution of a process zone to delamination resistance is independent of the loading mode in which it is created and solicited, neglecting the loading mode history. The impact of this modeling error on delamination prediction accuracy was analyzed, revealing a gap in existing literature as no model has addressed this problem yet.

To enhance this aspect, there is a need to experimentally quantify the ability of a partially developed process zone to resist delamination under a different loading mode, considering both static and fatigue loading. This involves forming a process zone under specific loading conditions, and subsequently measuring its fracture toughness under a different loading condition. This experimental approach allows for a more accurate consideration of loading history when interpolating the $\mathcal{R}$-curve between different loading modes.

In the transition between static and fatigue loading, accurate results were observed when shifting from mode I static loading to fatigue shear loading. Notably, the error induced by the mode interpolation present after the mode I static prediction was automatically corrected after 5000 fatigue cycles.

In conclusion, the presented modeling and simulation methodology demonstrates the capability of predicting static and fatigue delamination, accounting for $\mathcal{R}$-curve effects and damage process zones with non-self-similar evolution. However, it is crucial to be cautious when changing the loading mode conditions with an already-developed process zone.

CRediT authorship contribution statement

I. Leciñana: Writing – original draft, Validation, Software, Methodology, Investigation, Conceptualization. **L. Carreras:** Writing – review & editing, Supervision, Methodology, Investigation, Conceptualization. **J. Renart:** Writing – review & editing, Supervision, Methodology, Conceptualization. **J. Zurbitu:** Writing – review & editing, Supervision, Methodology, Conceptualization. **B.H.A.H. Tijs:** Writing – review & editing, Supervision, Conceptualization. **A. Turon:** Writing – review & editing, Supervision, Methodology, Conceptualization.

Declaration of competing interest

The authors declare the following financial interests/personal relationships which may be considered as potential competing interests: Albert Turon reports financial support was provided by Generalitat de Catalunya Ministry of Research and Universities. Laura Carreras reports financial support was provided by European Union. Jordi Renart reports financial support was provided by Generalitat de Catalunya Ministry of Research and Universites. If there are other authors, they declare that they have no known competing financial interests or personal relationships that could have appeared to influence the work reported in this paper.

Data availability

Data will be made available on request.

Acknowledgments

This work has been partially funded by the Spanish Ministry of Universities (Ministerio de Ciencia e Innovacion) through the Proyectos de Generacio'n de Conocimiento 2021, cofunded with FEDER (European Regional Development Fund) resources, under the project PID2021-127879OB-C21. LC acknowledges grant RYC2021-032171-I funded by MCIN/AEI/10.13039/501100011033 and by "European Union NextGeneration EU/PRTR". AT acknowledges the Generalitat de Catalunya for the ICREA Academia Prize 2022.

References

[1] Miracle DB, Donaldson SL, editors. ASM handbook volume 21: composites. ASM International; 2001, p. 1201.
[2] Tijs BH, Abdel-Monsef S, Renart J, Turon A, Bisagni C. Characterization and analysis of the interlaminar behavior of thermoplastic composites considering fiber bridging and R-curve effects. Composites A 2022;162:107101. http://dx.doi.org/10.1016/j.compositesa.2022.107101.
[3] Tijs BH, Lopes CS, Turon A, Bisagni C, Waleson J, van Ingen JW, Veldman SL. Virtual testing of thermoplastic composites: Towards a hybrid simulation-physical testing pyramid. In: ECCM 2018 - 18th European conference on composite materials. 2018.
[4] Falcó O, Ávila RL, Tijs B, Lopes CS. Modelling and simulation methodology for unidirectional composite laminates in a Virtual Test Lab framework. Compos Struct 2018;190(February):137–59. http://dx.doi.org/10.1016/j.compstruct.2018.02.016.
[5] Carreras L, Bak BL, Turon A, Renart J, Lindgaard E. Point-wise evaluation of the growth driving direction for arbitrarily shaped delamination fronts using cohesive elements. Eur J Mech A Solids 2018;72(October 2017):464–82. http://dx.doi.org/10.1016/j.euromechsol.2018.05.006.
[6] Dugdale D. Yielding of steel sheets containing slits. J Mech Phys Solids 1960;8(2):100–4. http://dx.doi.org/10.1016/0022-5096(60)90013-2.
[7] Rybicki EF, Kanninen MF. A finite element calculation of stress intensity factors by a modified crack closure integral. Eng Fract Mech 1977;9(4):931–8. http://dx.doi.org/10.1016/0013-7944(77)90013-3.
[8] Krueger R. Virtual crack closure technique: History, approach, and applications. Appl Mech Rev 2004;57(1–6):109–43. http://dx.doi.org/10.1115/1.1595677.
[9] Manoharan MG, Sun CT. Strain energy release rates of an interfacial crack between two anisotropic solids under uniform axial strain. Compos Sci Technol 1990;39(2):99–116. http://dx.doi.org/10.1016/0266-3538(90)90049-B.
[10] Turon A, Camanho PP, Costa J, Dávila CG. A damage model for the simulation of delamination in advanced composites under variable-mode loading. Mech Mater 2006;38(11):1072–89. http://dx.doi.org/10.1016/j.mechmat.2005.10.003.
[11] Turon A, Camanho PP, Costa J, Renart J. Accurate simulation of delamination growth under mixed-mode loading using cohesive elements: Definition of interlaminar strengths and elastic stiffness. Compos Struct 2010;92(8):1857–64. http://dx.doi.org/10.1016/j.compstruct.2010.01.012.
[12] Turon A, González EV, Sarrado C, Guillamet G, Maimí P. Accurate simulation of delamination under mixed-mode loading using a cohesive model with a mode-dependent penalty sti ff ness. Compos Struct 2018;184(October 2018):506–11. http://dx.doi.org/10.1016/j.compstruct.2017.10.017.
[13] Abdel-Monsef S, Tijs BH, Renart J, Turon A. Accurate simulation of delamination under mixed-mode loading using a multilinear cohesive law. Eng Fract Mech 2023;284(March):109233. http://dx.doi.org/10.1016/j.engfracmech.2023.109233.
[14] Sørensen BF, Jacobsen TK. Determination of cohesive laws by the J integral approach. Eng Fract Mech 2003;70(14):1841–58. http://dx.doi.org/10.1016/S0013-7944(03)00127-9.
[15] Sørensen BF, Kirkegaard P. Determination of mixed mode cohesive laws. Eng Fract Mech 2006;73(17):2642–61. http://dx.doi.org/10.1016/j.engfracmech.2006.04.006.
[16] Arrese A, Boyano A, De Gracia J, Mujika F. A novel procedure to determine the cohesive law in DCB tests. Compos Sci Technol 2017;152:76–84. http://dx.doi.org/10.1016/j.compscitech.2017.09.012.
[17] Arrese A, Insausti N, Mujika F, Perez-Galmés M, Renart J. A novel experimental procedure to determine the cohesive law in ENF tests. Compos Sci Technol 2019;170(October 2018):42–50. http://dx.doi.org/10.1016/j.compscitech.2018.11.031.
[18] Arrese A, Adarraga I, Insausti N, Renart J, Sarrado C. Mode II cohesive law extrapolation procedure of composite bonded joints. Eng Fract Mech 2021;244(January):107563. http://dx.doi.org/10.1016/j.engfracmech.2021.107563.
[19] Abdel Monsef S, Ortega A, Turon A, Maimí P, Renart J. An efficient method to extract a mode I cohesive law for bonded joints using the double cantilever beam test. Composites B 2019;178(September):107424. http://dx.doi.org/10.1016/j.compositesb.2019.107424.
[20] Abdel Monsef S, Pérez-Galmés M, Renart J, Turon A, Maimí P. The influence of mode II test configuration on the cohesive law of bonded joints. Compos Struct 2020;234(August 2019). http://dx.doi.org/10.1016/j.compstruct.2019.111689.
[21] Jensen SM, Martos MJ, Bak BL, Lindgaard E. Formulation of a mixed-mode multilinear cohesive zone law in an interface finite element for modelling delamination with R-curve effects. Compos Struct 2019;216(December 2018):477–86. http://dx.doi.org/10.1016/j.compstruct.2019.02.029.
[22] Farmand-Ashtiani E, Alanis D, Cugnoni J, Botsis J. Delamination in cross-ply laminates: Identification of traction-separation relations and cohesive zone modeling. Compos Sci Technol 2015;119:85–92. http://dx.doi.org/10.1016/j.compscitech.2015.09.025.
[23] Shen B, Stanciulescu I, Paulino GH. Inverse computation of cohesive fracture properties from displacement fields. Inverse Probl Sci Eng 2010;18(8):1103–28. http://dx.doi.org/10.1080/17415977.2010.512661.
[24] Bouhala L, Makradi A, Belouettar S, Younes A, Natarajan S. An XFEM/CZM based inverse method for identification of composite failure parameters. Comput Struct 2015;153:91–7. http://dx.doi.org/10.1016/j.compstruc.2015.02.035.
[25] Valoroso N, Sessa S, Lepore M, Cricrì G. Identification of mode-I cohesive parameters for bonded interfaces based on DCB test. Eng Fract Mech 2013;104:56–79. http://dx.doi.org/10.1016/j.engfracmech.2013.02.008.
[26] Pereira FA, Morais JJ, de Moura MF, Dourado N, Dias MI. Evaluation of bone cohesive laws using an inverse method applied to the DCB test. Eng Fract Mech 2012;96:724–36. http://dx.doi.org/10.1016/j.engfracmech.2012.10.002.
[27] Robinson P, Galvanetto U, Tumino D, Bellucci G, Violeau D. Numerical simulation of fatigue-driven delamination using interface elements. Internat J Numer Methods Engrg 2005;63(13):1824–48. http://dx.doi.org/10.1002/nme.1338.
[28] Turon A, Costa J, Camanho PP, Dávila CG. Simulation of delamination in composites under high-cycle fatigue. Composites A 2007;38(11):2270–82. http://dx.doi.org/10.1016/j.compositesa.2006.11.009.
[29] Harper PW, Hallett SR. A fatigue degradation law for cohesive interface elements - Development and application to composite materials. Int J Fatigue 2010;32(11):1774–87. http://dx.doi.org/10.1016/j.ijfatigue.2010.04.006.
[30] Pirondi A, Moroni F. Simulation of mixed-mode I/II fatigue crack propagation in adhesive joints with a modified cohesive zone model. J Adhes Sci Technol 2011;25(18):2483–99. http://dx.doi.org/10.1163/016942411X580180.
[31] Kawashita LF, Hallett SR. A crack tip tracking algorithm for cohesive interface element analysis of fatigue delamination propagation in composite materials. Int J Solids Struct 2012;49(21):2898–913. http://dx.doi.org/10.1016/j.ijsolstr.2012.03.034.
[32] Brian V, Bak L, Turon A, Lindgaard E, Lund E. A simulation method for high-cycle fatigue-driven delamination using a cohesive zone model. Internat J Numer Methods Engrg 2016;106:1102–19. http://dx.doi.org/10.1002/nme, URL: http://onlinelibrary.wiley.com/doi/10.1002/nme.3279/full.
[33] Carreras L, Turon A, Bak BL, Lindgaard E, Renart J, Martin de la Escalera F, Essa Y. A simulation method for fatigue-driven delamination in layered structures involving non-negligible fracture process zones and arbitrarily shaped crack fronts. Composites A 2019;122(January):107–19. http://dx.doi.org/10.1016/j.compositesa.2019.04.026, arXiv:1905.05000.

[34] Dávila CG. From S-N to the Paris law with a new mixed-mode cohesive fatigue model for delamination in composites. Theor Appl Fract Mech 2020;106(June). http://dx.doi.org/10.1016/j.tafmec.2020.102499.
[35] Dávila CG, Rose CA, Murri GB, Jackson WC, Johnston WM. Evaluation of fatigue damage accumulation functions for delamination initiation and propagation. Tech. rep. Nasa/tp–2020-220584, NASA; 2020.
[36] Lecinana I, Zurbitu J, Renart J, Turon A, Carreras L. Global sensitivity analysis of an S-N curve-based fatigue cohesive zone model and validation through a benchmark test. In: 20th European conference on composite materials. 2022.
[37] Leciñana I, Zurbitu J, Renart J, Turon A. A robust fatigue parameter determination method for a local fatigue cohesive zone model. Int J Fatigue 2023;171(February). http://dx.doi.org/10.1016/j.ijfatigue.2023.107582.
[38] Dávila CG, Rose CA, Camanho PP. A procedure for superposing linear cohesive laws to represent multiple damage mechanisms in the fracture of composites. Int J Fract 2009;158(2):211–23. http://dx.doi.org/10.1007/s10704-009-9366-z.
[39] Greenhalgh ES. Failure analysis and fractography of polymer composites. 2009, p. 595. http://dx.doi.org/10.1533/9781845696818.
[40] Ferreira Motta R, Alderliesten R, Zarouchas D, Yutaka Shiino M, Odila Hilario Cioffi M, Jacobus Cornelis Voorwald H. Explaining the multiple energy thresholds for damage mechanisms activation in laminate composites under cyclic loadings. Composites A 2023;167(September 2022). http://dx.doi.org/10.1016/j.compositesa.2023.107451.
[41] Ferreira Motta R, Alderliesten R, Yutaka Shiino M, Odila Hilário Cioffi M, Jacobus Cornelis Voorwald H. Scrutinizing interlaminar fatigue loading cycle in composites using acoustic emission technique: Stress ratio influence on damage formation. Composites A 2020;138(May):1–11. http://dx.doi.org/10.1016/j.compositesa.2020.106065.
[42] Carreras L, Bak B, Jensen S, Lequesne C, Xiong H, Lindgaard E. Benchmark test for mode I fatigue-driven delamination in GFRP composite laminates: Experimental results and simulation with the inter-laminar damage model implemented in SAMCEF. Composites B 2023;253(December 2022):110529. http://dx.doi.org/10.1016/j.compositesb.2023.110529.
[43] Jensen SM, Bak BL, Bender JJ, Lindgaard E. Transition-behaviours in fatigue-driven delamination of GFRP laminates following step changes in block amplitude loading. Int J Fatigue 2021;144(June 2020):106045. http://dx.doi.org/10.1016/j.ijfatigue.2020.106045.
[44] Jensen SM, Bak BL, Bender JJ, Carreras L, Lindgaard E. Transient delamination growth in GFRP laminates with fibre bridging under variable amplitude loading in G-control. Composites B 2021;225(September):109296. http://dx.doi.org/10.1016/j.compositesb.2021.109296.
[45] Leciñana I, Renart J, Carreras L, Turon A, Zurbitu J, Tijs B. A fatigue test based on inclined loading block concept to benchmark delamination growth considering loading history and R-curve effect. Composites A 2024;181:108128. http://dx.doi.org/10.1016/j.compositesa.2024.108128.
[46] Lecinana I, Renart J, Turon A, Zurbitu J, Tijs B. Characterization and analysis of the mode I interlaminar fatigue behaviour of thermoplastic composites considering R-curve effects. Eng Fract Mech 2023;286(June). http://dx.doi.org/10.1016/j.engfracmech.2023.109273.
[47] Abdel Monsef S, Ortega A, Turon A, Maimí P, Renart J. An efficient method to extract a mode I cohesive law for bonded joints using the double cantilever beam test. Composites B 2019;178(August):107424. http://dx.doi.org/10.1016/j.compositesb.2019.107424.
[48] Abdel Monsef S, Pérez-Galmés M, Renart J, Turon A, Maimí P. The influence of mode II test configuration on the cohesive law of bonded joints. Compos Struct 2020;234(August). http://dx.doi.org/10.1016/j.compstruct.2019.111689.
[49] Allegri G, Wisnom MR. A non-linear damage evolution model for mode II fatigue delamination onset and growth. Int J Fatigue 2012;43:226–34. http://dx.doi.org/10.1016/j.ijfatigue.2012.03.016.
[50] Yin S, Gong Y, Li W, Zhao L, Zhang J, Hu N. A novel four-linear cohesive law for the delamination simulation in composite DCB laminates. Composites B 2020;180:107526. http://dx.doi.org/10.1016/j.compositesb.2019.107526.
[51] Joosten MW, Dávila CG, Yang Q. Predicting fatigue damage in composites subjected to general loading conditions. Composites A 2022;156(February). http://dx.doi.org/10.1016/j.compositesa.2022.106862.
[52] Tijs BH, Doldersum MH, Turon A, Waleson JE, Bisagni C. Experimental and numerical evaluation of conduction welded thermoplastic composite joints. Compos Struct 2022;281(November 2021):114964. http://dx.doi.org/10.1016/j.compstruct.2021.114964.
[53] Renart J, Leciñana I, Tijs B, Turón A, Zurbitu J. Characterization and analysis of the mode II interlaminar fatigue behaviour of thermoplastic composites considering R-curve effects. 2024, in preparation.
[54] ASTM Standards. ASTM D5528/D5528M-21: Standard test method for mode I interlaminar fracture toughness of unidirectional fiber-reinforced polymer matrix composites. In: Book of standards, vol. 15.03, 2021, http://dx.doi.org/10.1520/D5528_D5528M-21.
[55] ISO Standards. ISO 15114:2014 Fibre-reinforced plastic composites — Determination of the mode II fracture resistance for unidirectionally reinforced materials using the calibrated end-loaded split (C-ELS) test and an effective crack length approach. 2014.
[56] Pérez-Galmés M, Renart J, Sarrado C, Brunner AJ, Rodríguez-Bellido A. Towards a consensus on mode II adhesive fracture testing: Experimental study. Theor Appl Fract Mech 2018;98:210–9. http://dx.doi.org/10.1016/j.tafmec.2018.09.014.
[57] Daneshjoo Z, Shokrieh MM, Fakoor M. A micromechanical model for prediction of mixed mode I/II delamination of laminated composites considering fiber bridging effects. Theor Appl Fract Mech 2018;94(January):46–56. http://dx.doi.org/10.1016/j.tafmec.2017.12.002.
[58] Gong Y, Zhao L, Zhang J, Wang Y, Hu N. Delamination propagation criterion including the effect of fiber bridging for mixed-mode I/II delamination in CFRP multidirectional laminates. Compos Sci Technol 2017;151:302–9. http://dx.doi.org/10.1016/j.compscitech.2017.09.002.
[59] Shokrieh MM, Zeinedini A, Ghoreishi SM. On the mixed mode I/II delamination R-curve of E-glass/epoxy laminated composites. Compos Struct 2017;171:19–31. http://dx.doi.org/10.1016/j.compstruct.2017.03.017.